Applied Physics A (2018) 124:817
https://doi.org/10.1007/s00339-018-2244-7

Applied Physics A
Materials Science & Processing

Enhanced NO_2 gas-sensing performance of Pd/ZnO-codecorated SnO_2 nanorod sensors

Seung-Bok Choi[1] · Woo Seok Lee[2] · Chongmu Lee[2] · Sangmin Lee[3]

Received: 6 July 2018 / Accepted: 8 November 2018 / Published online: 13 November 2018

Abstract
SnO_2 nanorods codecorated with Pd and ZnO were synthesized using a three-step process involving: the synthesis of SnO_2 nanorods by the thermal evaporation of Sn powders followed by the sol–gel deposition of ZnO and Pd nanoparticles. The NO_2 gas-sensing properties of the nanorods were examined. The nanorods were composed of primitive tetragonal-structured single crystal SnO_2, while the ZnO and Pd nanoparticles were composed of wurtzite-structured ZnO single crystal and face-centered cubic-structured Pd single crystal, respectively. The Pd/ZnO-codecorated SnO_2 nanorod sensors showed a remarkably enhanced response to NO_2 compared to either ZnO or Pd-decorated SnO_2 nanorod sensors. The responses of multiple networked Pd/ZnO-decorated SnO_2 nanorod sensors were increased four to fivefold at NO_2 concentrations ranging from 1 to 5 ppm Pd/ZnO-decorated SnO_2 nanorod sensors which also showed shorter response and recovery times and higher selectivity than with ZnO or Pd-decorated SnO_2 nanorod sensors. The NO_2 sensing mechanism of the Pd/ZnO-codecorated SnO_2 nanorods is also discussed.

1 Introduction

Nitrogen dioxide (NO_2) is one of the most dangerous gases and has a noxious influence on humans and the environment. NO_2 is mainly introduced into the air from the exhaust fumes of automobiles and power plants and can cause damage to the lungs and cardiovascular system. In addition, it causes air pollution when sun light separates NO_2 into NO and O generating ground-level ozone as well as photochemical smog [1–3]. Because of its harmful nature, various efforts have been made to develop effective NO_2 gas sensors which can detect low concentrations of the gas with low operating costs and high sensitivity.

Semiconducting metal oxides (SMO) are the most widely used materials for gas sensors. However, while SMO-based gas sensors have many advantages such as high sensitivity, they also have disadvantages such as high operating temperature, poor selectivity and poor reliability. To overcome these problems, researchers have developed techniques such as metal catalyst doping [4–9], heterostructure formation [10–12] and UV light irradiation [13–15]. Among these techniques, heterostructure formation might be the strategy most widely studied over the last decade. The improvements achieved by heterostructure formation include higher gas sensitivity, shorter sensing time and higher selectivity.

Many studies on heterostructure sensors have focussed more on the detection of reducing gases than oxidizing gases because most sensing materials show stronger response to reducing gases. This might be due mainly to the following two effects: (1) the electronic effect, which results in a larger decrease in resistance upon exposure to reducing gas compared to a small increase in resistance upon exposure to oxidizing gas, leading to a stronger response of the sensor to reducing gases [16, 17] and (2) the chemical effect which results in enhanced oxidation of reducing gases due to the superior catalytic activity of the counterpart material in the composite structured sensor for the oxidation reaction [18–20]. Because of this reason, we must employ a stronger strategy in developing oxidizing gas sensors.

✉ Chongmu Lee
cmlee@inha.ac.kr

[1] Department of Mechanical Engineering, Inha University, 253 Yonghyun-dong, Nam-gu, Incheon 402-751, Republic of Korea

[2] Department of Materials Science and Engineering, Inha University, 253 Yonghyun-dong, Nam-gu, Incheon 402-751, Republic of Korea

[3] Department of Electronic Engineering, Inha University, 253 Yonghyun-dong, Nam-gu, Incheon 402-751, Republic of Korea

Considering these points, we decided to develop an NO_2 gas sensor with high performance by combining two different techniques: metal catalyst doping and n–n heterostructure formation. There are numerous reports on the influence of one of the above two techniques on the sensing properties of SnO_2 nanorod sensors, but there are only a few reports on the influence of a combination of the two techniques [21–24]. In this study, we combined two techniques: metal catalyst doping and n–n heterostructure formation to develop a NO_2 gas sensor with high performance. We adopted ZnO-decorated SnO_2 nanorods as basic sensing materials first and then Pd doping as an additional technique. Moreover, ZnO-decorated SnO_2 is anticipated to show better sensing performance toward oxidizing gases than reducing gases,because ZnO has a larger work function than SnO_2 [25–27]. We compared the sensing properties of pristine SnO_2 nanorods, Pd-decorated SnO_2, ZnO-decorated SnO_2, and Pd/ZnO-codecorated nanorods. In addition, we discuss the sensing mechanism of the Pd/ZnO-codecorated nanorods toward oxidizing gas NO_2 based on the potential barrier-controlled carrier transport model combined with the surface depletion model.

2 Experiments

2.1 Synthesis of SnO_2 nanorods

SnO_2 nanorods were synthesized by vapor–liquid–solid growth of tin powders with a purity of 99.99%. A 3-nm-thick Au thin film was deposited on p-type (100) Si substrates using DC sputtering. A quartz tube was mounted horizontally inside a tube furnace and an alumina boat with Sn powders was placed at the center of the quartz tube. The Au-deposited Si substrate was placed ~ 5 mm away from the alumina boat. The furnace was heated to 900 °C at a heating rate of 10 °C/min. A gas mixture composed of N_2 (300 sccm) and O_2 (10 sccm) flowed at a constant total pressure of 1 Torr. The evaporation process was maintained for 1 h.

2.2 Synthesis of Pd and ZnO nanoparticle-decorated SnO_2 nanorods

For the synthesis of ZnO nanoparticles, zinc nitrate hexahydrate $Zn(NO_3)_2{\cdot}6H_2O$ and sodium hydroxide (NaOH) were used as precursors [28]. ZnO nanoparticles were produced by the following reactions [29]:

$$Zn\left(NO_3\right)_2 \rightarrow Zn^{2+} + 2NO_3^-, \quad (1)$$

$$Zn_2^+ + 2OH^- \rightarrow Zn(OH)_2, \quad (2)$$

$$Zn(OH)_2 \rightarrow ZnO + H_2O. \quad (3)$$

To prepare the precursor solution, 1.5 g of zinc nitrate hexahydrate was dissolved in 50 mL deionized water and was mixed with a mixture of NaOH (4 mL) and deionized water solution(90 mL) using ultrasonic vibrations. The obtained solution was heated at 120 °C for 24 h in an oven and dripped onto the SnO_2 nanorods.

Subsequently, the synthesized ZnO nanoparticle-decorated SnO_2 nanorods were immersed in an ethanol/$PdCl_2$ solution, followed by UV laser ($\lambda = 254$ nm, $I = 1.2$ mW/cm^2) irradiation for 30 min. After that, the samples were calcined at 600 °C for 1 h in a N_2 atmosphere with a flow rate of 100 sccm and a pressure of 1 Torr.

2.3 Characterization

To observe and compare the morphology of three different types of samples(pristine SnO_2 nanorods,ZnO nanoparticle-decorated SnO_2 nanorods and Pt/ZnO nanoparticle-decorated SnO_2 nanorods), field-emission scanning electron microscopy (FE-SEM, Hitach S-4300SE, Japan) and transmission electron microscopy (TEM, Philips CM-200) combined with an energy-dispersive X-ray spectrometry (EDS) were used to examine the morphology and structure of the samples. The crystal structure was determined by glancing-angle X-ray diffraction (XRD, Philips X'pert MRD diffractometer) using Cu–K_α radiation (0.154 nm) at a scan rate of 4°/min and 0.5° glancing angle with a rotating detector.

2.4 Gas-sensing test

Sensors were prepared on the SiO_2-grown Si (100) substrates equipped with pairs of interdigitated Ni (200 nm)/Au (50 μm) electrodes fabricated by sputter deposition followed by photolithography. The nanorod samples(5 g)were dispersed ultrasonically in isopropyl alcohol (5 mL) and placed onto the interdigited electronic (IDE) pattern. A flow-through technique was used for measuring the gas-sensing properties in a temperature-stabilized chamber. The sensors were mounted in a quartz tube with an electrical feedthrough and its resistance was measured using a home-built computer consisting of a test chamber, sensor holder, Keithley Source Meter-2612, mass flow controllers and a data acquisition system. During the test, NO_2 gas was injected into the quartz tube at concentrations of 2.5, 5, 25, 50, or 100 ppm to obtain the desired concentration. The sensing tests were then conducted at room temperature and 40% RH using a voltamperometric method. The electrical resistance of the gas sensors was determined at 300 °C by measuring the electric current using a Keithley Source Meter-2612 under a constant applied voltage of 1 V. Detailed procedures of the sensor device fabrication and sensing tests are described elsewhere [30].

The response was defined as $[R_g/R_a]$ for NO_2 gas, where $R_g$and R_a are the electrical resistances of the sensors in NO_2 gas and air, respectively. The response and recovery times were defined as the times to reach 90% of the resistance change upon exposure to NO_2 and air, respectively.

3 Results and discussion

SEM images of pristine SnO_2 nanorods, ZnO nanoparticle-decorated SnO_2 and Pd/ZnO nanoparticle-codecorated SnO_2 nanorods are presented in Fig. 1a–d. Pristine SnO_2 nanorods have rod-like morphologies with smooth surfaces. The mean diameter of the SnO_2 nanorods was ~ 100 nm and the lengths of SnO_2 nanorods ranged up to a few tens of micrometers (Fig. 1a). The diameters of the Pd nanoparticles in the Pd-decorated SnO_2 nanorods ranged from 5 to10 nm (Fig. 1b), whereas the diameters ofZnO nanoparticles in the ZnO-decorated SnO_2 nanorods ranged from 10 to 25 nm (Fig. 1c). The diameters of the Pd and ZnO nanoparticles on the Pd/ZnO-codecorated SnO_2 nanorods were in ranges of 5–10 nm and 10–25 nm, respectively (Fig. 1d). However, the average diameter of the ZnO particles is approximately three times as large as that of Pt particles. It is interesting that the Pd nanoparticles tend to be distributed separately from the ZnO nanoparticles. Accordingly, ZnO and Pd nanoparticles do not contact with each other directly. In contrast, the Pd nanoparticles make contact directly with the SnO_2.

Figure 2a–d show the TEM images and corresponding electron diffraction patterns of the SnO_2 nanorods codecorated with Pd and ZnO nanoparticles. Figure 2a, b present low- and medium-magnification TEM images of the Pd/ZnO nanoparticle-codecorated SnO_2 nanorods. The diameters of the ZnO nanoparticles were three to tenfold larger than those of the Pd nanoparticles, as shown in Fig. 2a. A significant difference in numbers of Pd and CaO particles are noted between on SEM and TEM images. The numbers of Pd and CaO particles on the SnO_2 nanorod with a length of 100 nm, counted on a SEM image are approximately 25 and 20, respectively. In contrast, the numbers of Pd and CaO particles on the SnO_2 nanorod with a length of 1000 nm, counted on a SEM image are approximately 25 and 20, respectively. The smaller number of nanoparticles on the TEM image might be due to many particles being swept away by ethanol

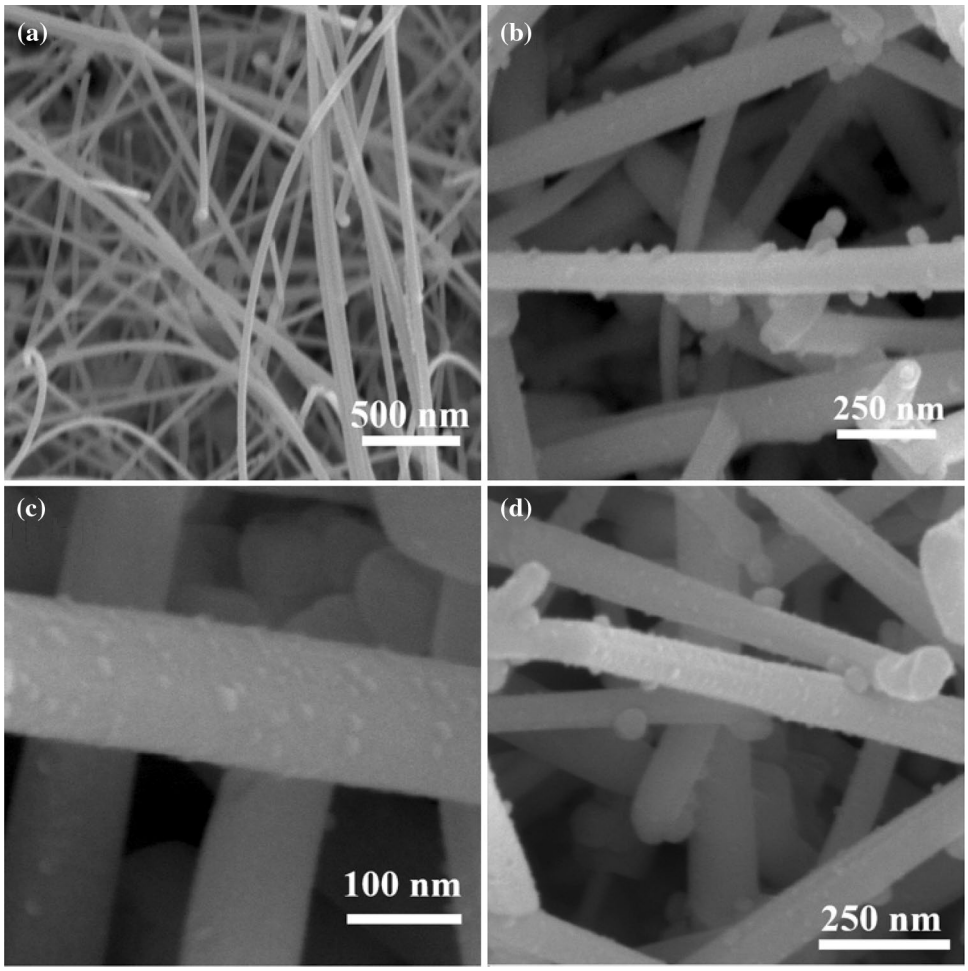

Fig. 1 **a** Low-magnification SEM images of a pristine SnO_2 nanorods, **b** ZnO-decorated SnO_2 nanorods, **c** Pd-decorated SnO_2 nanorods, and **d** Pd/ZnO-codecorated SnO_2 nanorods

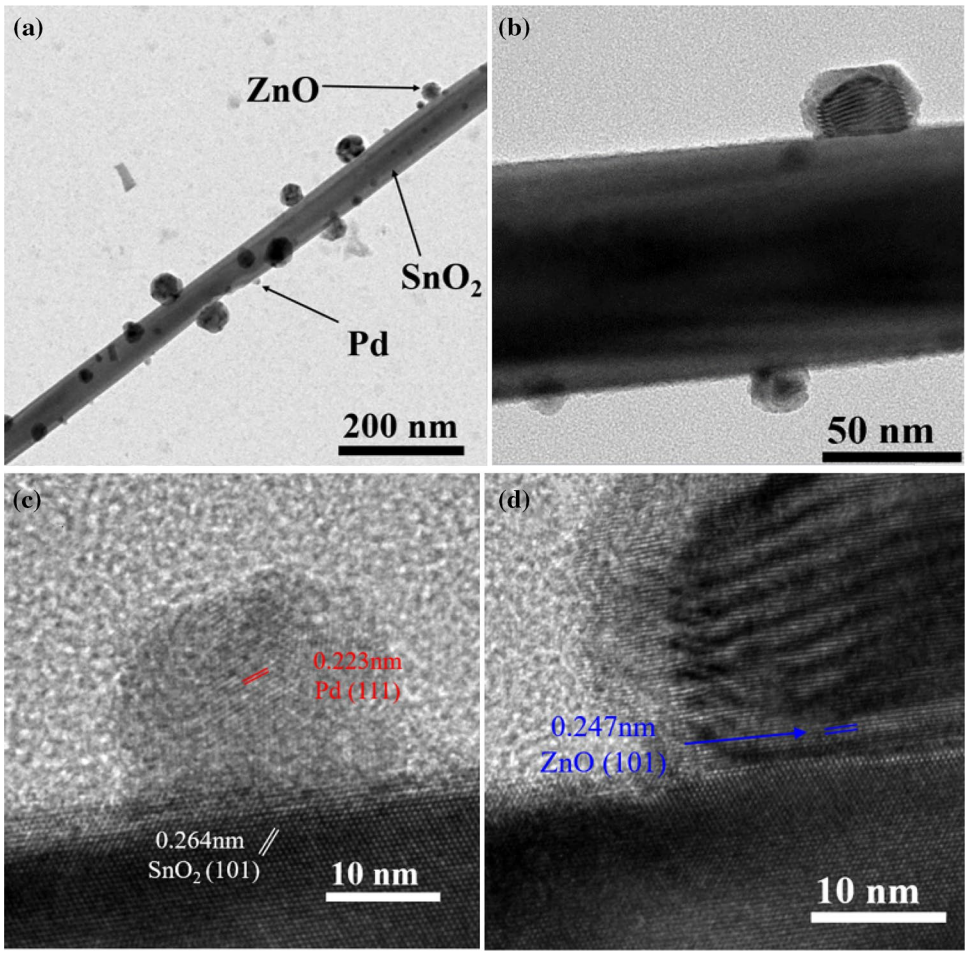

Fig. 2 **a** Low-magnification and **b** high-resolution TEM images of a typical Pd/ZnO-codecorated SnO_2 nanorod. **c** high-resolution TEM image of a typical Pd/ZnO-codecorated SnO_2 nanorod and **d** corresponding selected area electron diffraction (SAED) pattern

during TEM sample preparation. The existence of the fringe patterns in the Pd and ZnO nanoparticles as well as the SnO_2 nanorods in the high-resolution TEM (HRTEM) images (Fig. 2c, d) reveals that both the Pd and ZnO nanoparticles as well as the SnO_2 have high crystallinity, i.e., they are single crystals. The clear spots in the corresponding electron diffraction patterns confirm that the SnO_2 nanorods, and Pd and ZnO nanoparticles are single crystals (Fig. 2d). An EDS elemental microanalysis of typical Pd and ZnO nanoparticle-codecorated SnO_2 nanorods shown in Fig. 3a confirms that the sample is composed of Sn (28.20 at%), O (50.77 at%), Zn (13.45 at%) and Pd elements (7.58 at%). The XRD patterns of the pristine and Pd and ZnO-codecorated SnO_2 nanorod samples are presented in Fig. 3b. The sharp peaks in the XRD pattern of the pristine SnO_2 nanorods were assigned to (110), (101), (200), and (002) reflections of tetragonal-structured SnO_2 (JCPDS No. 41-1445). The additional peaks in the Pd and ZnO-codecorated SnO_2 nanorod sample fit well with face-centered cubic-structured Pd (JCPDS N. 46-1043)and wurtzite-structured ZnO(JCPDS No. 36-1451). The additional peaks were assigned to the (111), (200) and (220) reflections of Pd and (100), (002) and (102) reflections of ZnO.

Figure 4 presents the temperature dependence of the responses of the pristine SnO_2 nanorods and Pd/ZnO-codecorated SnO_2 nanorods on the operating temperature to NO_2. The pristine SnO_2 nanorods and Pd/ZnO-codecorated SnO_2 nanorods showed maximal responses at 350 and 300 °C, respectively, suggesting that the optimal operating temperatures of the pristine SnO_2 nanorods and Pd/ZnO-codecorated SnO_2 nanorods are 350 and 300 °C, respectively. The lower operating temperature of the Pd/ZnO-codecorated SnO_2 nanorods than that of the pristine SnO_2 nanorods is also one of the advantages of the former nanostructures. Hereafter, all the sensing data were obtained at 350 °C in this study. Figure 5a–d present the dynamic response curves of the four different types of samples toward NO_2 gas at 300 °C: the pristine SnO_2 nanorods, ZnO-decorated SnO_2 nanorods, and Pd-decorated SnO_2 nanorods, and Pd/ZnO-codecorated SnO_2 nanorods, respectively, towards NO_2 gas, respectively. The dynamic response curves showed somewhat unstable but reproducible response and recovery characteristics. Figure 6a presents the responses of the four different types of samples as a function of the NO_2 concentration. The Pd/ZnO-codecorated SnO_2 nanorods showed the strongest response (5.52) to 5 ppm of NO_2, while the pristine SnO_2

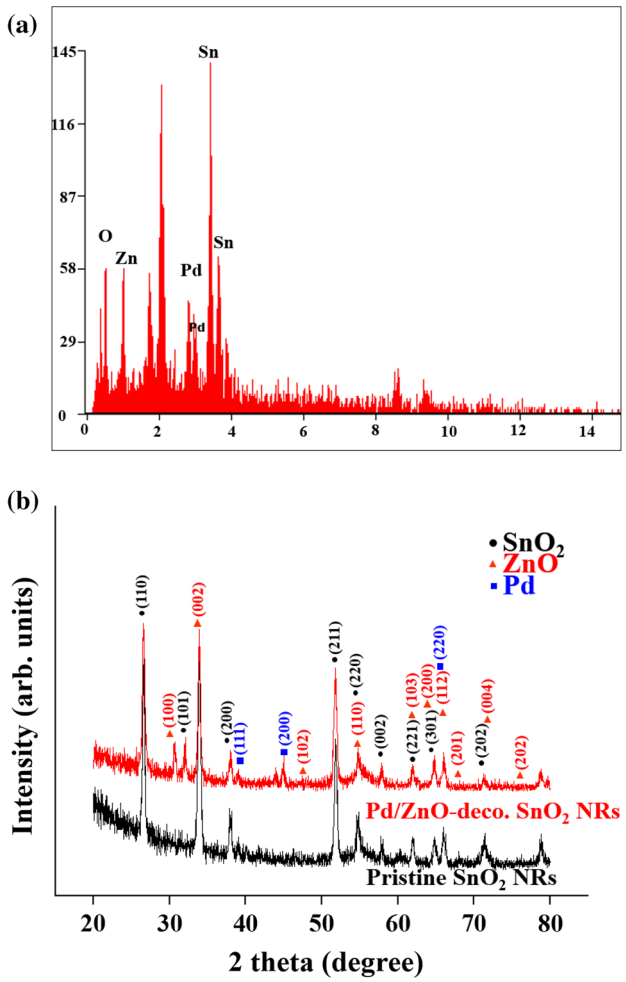

Fig. 3 **a** Energy-dispersive X-ray spectrum (EDS) of a typical Pd/ZnO-codecorated SnO_2 nanorods. **b** XRD patterns of pristine SnO_2 nanorods and Pd/ZnO-codecorated SnO_2 nanorods

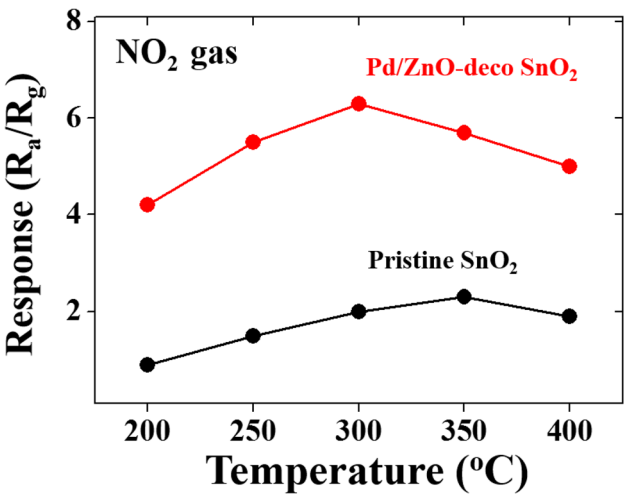

Fig. 4 Response of the Pd/ZnO-codecorated SnO_2 nanorods to an NO_2 concentration of 5 ppm as a function of operating temperature

nanorods showed the weakest response (2.28). The Pd/ZnO-codecorated SnO_2 nanorod sensor also showed faster response and recovery than the pristine SnO_2 nanorod sensor for the same NO_2 concentration (Fig. 6b, c). A comparison of the response and recovery times between the pristine and Pd/ZnO-codecorated nanorod sensors showed that the response and recovery times of the SnO_2 nanorod sensor for 5 ppm of NO_2 were reduced from 21.1 to 17.74 s and from 75 to 60 s, respectively, by Pd and ZnO codecoration. Decoration of ZnO enhances the NO_2 gas-sensing properties through only electronic mechanism, but the enhancing effect is significant because of the combination of two electronic mechanisms: modulation of conduction channel and modulation of barrier height at the ZnO/SnO_2 contact. In contrast, Pd particles enhance the NO_2 gas-sensing properties through two mechanisms: electronic and chemical mechanisms. Regarding the electronic mechanism, effects of modulation of conduction channel and modulation of barrier height are not as strong as those of ZnO particles. However, the chemical effects such as adsorption of O_2 and NO_2 molecules and dissociation of NO_2 desorption of the reaction products are enhanced because of the role of Pd as a catalyst.

In general, the recovery time decreases with increase in the gas concentration. In contrast, in this study they do not change with increasing the NO_2 concentration except the lower concentration range. This phenomenon does not seem to be due to the leakage of gas line and sealing parts of tube furnace because the responses of the sensors tend to increase with increasing the NO_2 concentration. When the supply of NO_2 is on, a response occurs, whereas when the supply of NO_2 is off, recovery occurs. When NO_2 supply is off, the sensors are exposed to only air. This means response is related to NO_2, whereas recovery is related to air, i.e., O_2. Therefore, the recovery time is not as sensitive to the concentration of NO_2 as the response time.

The enhanced sensing performance of the Pd/ZnO-codecorated SnO_2 nanorod sensor compared to the pristine SnO_2 nanorod sensor can be explained mainly by electronic sensing mechanisms. A critical difference between the pristine and codecorated SnO_2 nanorod is the existence of Pd–SnO_2 and ZnO–SnO_2 interfaces in the latter. Two electronic sensing mechanisms based on the existence of these n–n junctions, i.e., modulation of the depletion layer width or conduction channel width at the heterojunction interface, and modulation of the interfacial potential barrier height, should be considered when explaining the enhanced sensing performance of the Pd and ZnO-codecorated SnO_2 nanorod sensor.

As we saw in Fig. 1a–d, Pd nanoparticles contact SnO_2 directly, but do not directly contact ZnO. Therefore, all the types of contacts which can explain the gas-sensing mechanism of the Pd/ZnO-codecorated SnO_2 nanorod sensor are ZnO–SnO_2 and Pd–SnO_2. Figure 7 shows energy band diagrams and top view schematics of a ZnO and

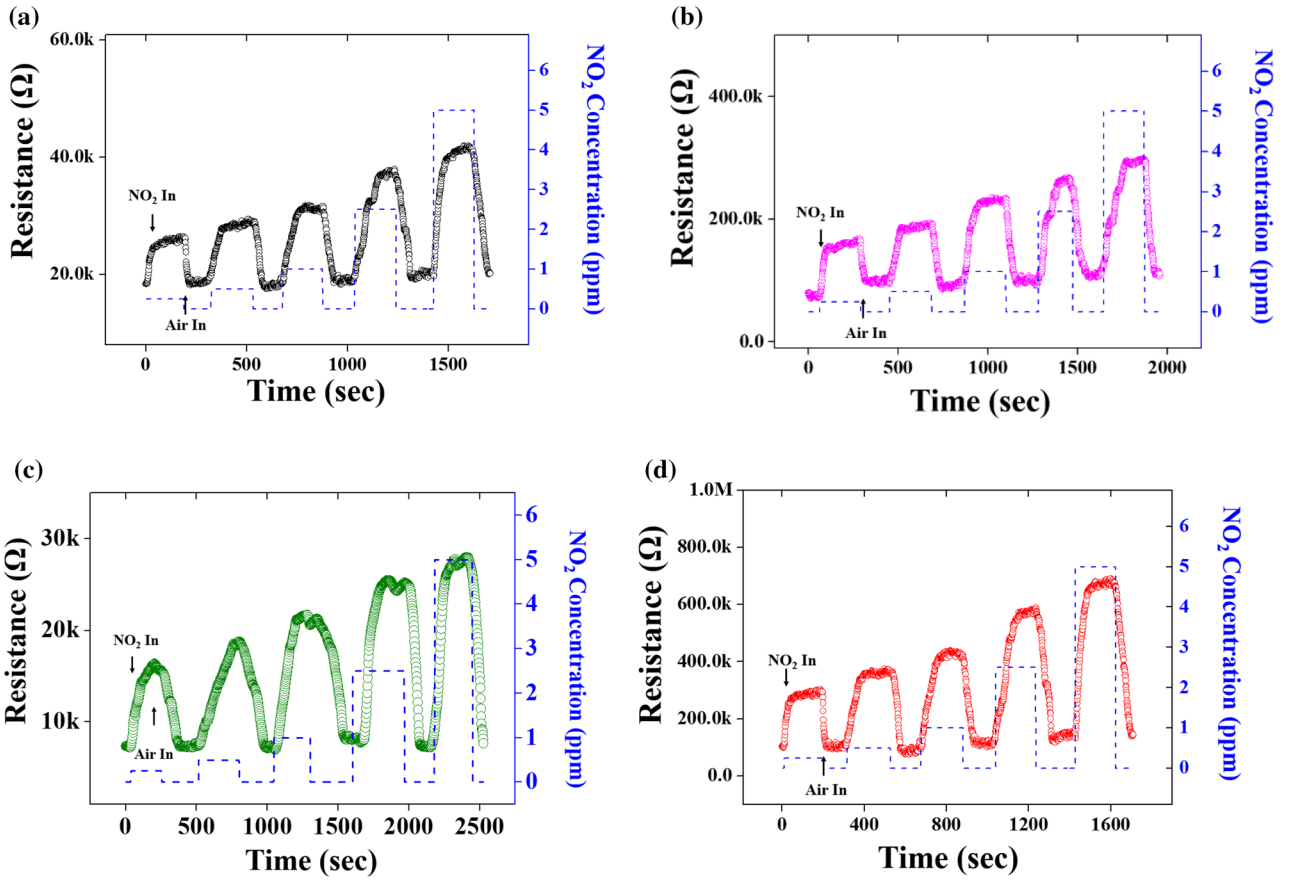

Fig. 5 Dynamic response curves of four different gas sensors fabricated from **a** pristine SnO_2 nanorods, **b** ZnO-decorated SnO_2 nanorods, **c** Pd-decorated SnO_2 nanorods, and **d** Pd/ZnO-codecorated SnO_2 nanorods

Pd-decorated SnO_2 nanorod depicting the depletion layer and conduction channel formed in vacuum, air and NO_2 gas at the ZnO–SnO_2 and Pd–SnO_2 interface and their adjacent regions. In a vacuum after contact, electron transfer occurs from SnO_2 to ZnO due to $E_F(SnO_2) > E_F(ZnO)$, resulting in the formation of thin depletion and accumulation layers on the ZnO and SnO_2 sides, respectively, near the ZnO–SnO_2 interface in the Pd/ZnO-codecorated SnO_2 nanorod. In air, more electrons transfer from the conduction bands of ZnO and SnO_2 to the adsorbed oxygen species and electrons are consumed to convert the adsorbed oxygen molecules to oxygen ions, depending on the operating temperature as follows [31]:

$$O_2(\text{gas}) + e^- \leftrightarrow O_2^-(\text{ads}), \tag{4}$$

$$O_2^-(\text{gas}) + e^- \leftrightarrow 2O^-(\text{ads}), \tag{5}$$

$$2O^-(\text{ads}) + e^- \leftrightarrow O^{2-}. \tag{6}$$

Consequently, depletion layers form on both SnO_2 and ZnO sides near the ZnO–SnO_2 interface. In addition to the depletion layer, a potential barrier with a height of E_1 also forms at the ZnO–SnO_2 interface.

Upon exposure to NO_2 gas, the following reactions occur [32–34]:

$$NO_2(\text{gas}) + e^- \rightarrow NO^{2-}(\text{ads}), \tag{7}$$

$$NO^{2-}(\text{ads}) + O^-(\text{ads}) + 2e^- \rightarrow NO(\text{gas}) + 2O^{2-}(\text{ads}), \tag{8}$$

$$NO(\text{gas}) + e^- \rightarrow NO^-(\text{ads}). \tag{9}$$

This reaction will expand the depletion layers further, i.e., thicker depletion layers form on both the SnO_2 and ZnO sides, respectively, in the interfacial region due to the transfer of more electrons from the conduction bands of ZnO and SnO_2 to the adsorbed oxygen species, and a smaller conduction channel width (W_2), leading to an increase in the resistance and thereby the enhanced electrical response of the nanorod sensor to the NO_2 gas. In addition to the depletion layer, a potential barrier with a height of E_2 also forms at the ZnO–SnO_2 interface. Because E_2 is larger than E_1, a

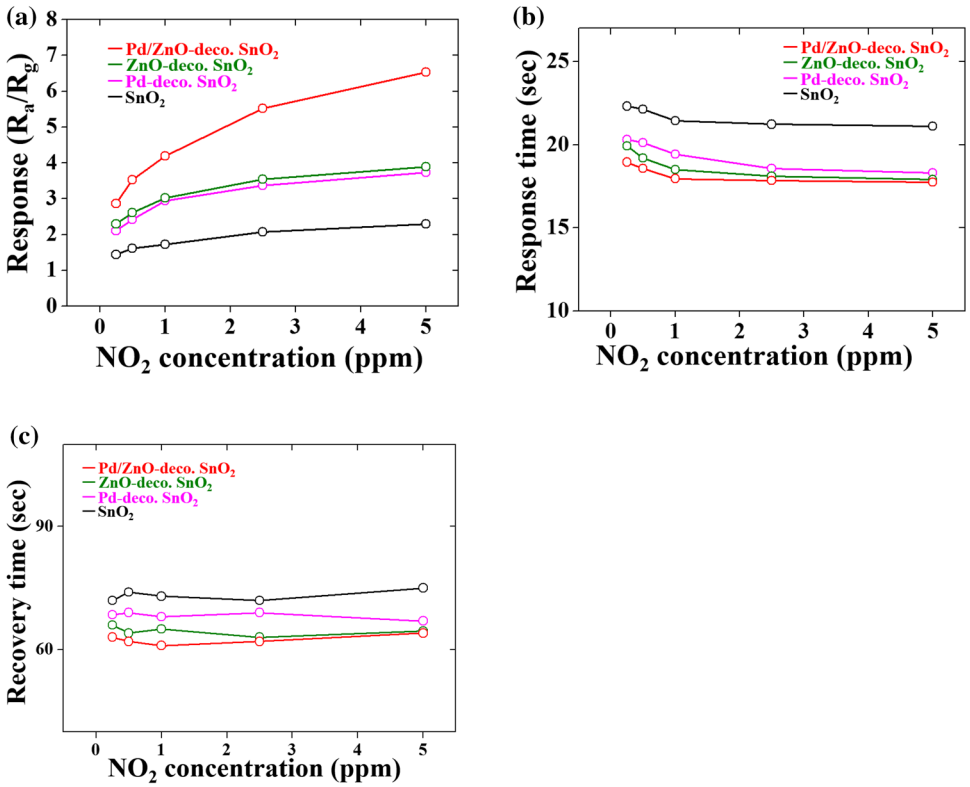

Fig. 6 **a** Responses, **b** response times and **c** recovery times of the multiple networked ZnSe nanowire gas sensor to NO_2 gas at 300 °C

larger potential modulation occurs in an NO_2 atmosphere than in air, leading to the enhanced electrical response of the nanorod sensor to the NO_2 gas.

On the other hand, the SnO_2 in contact with Pd forms a Schottky junction and helps to transfer more electrons in the case of Pd-decorated SnO_2 nanorods.The chemisorption and dissociation of NO_2 gas is enhanced on the Pd nanoparticle surface and NO_2 gas is spilt over the Pd nanoparticles [35] due to the highly catalytic or conductive nature of Pd [36]. Consequently, the number of electrons attracted to the gas increases.

Figure 8 compares the responses of the pristine SnO_2 nanorod sensor and Pd-decorated SnO_2 nanorod sensor to NO_2 with their responses to other gases. The Pd/ZnO-decorated SnO_2 nanorod sensor, notably, showed selectivity toward NO_2, whereas the pristine SnO_2 nanorod sensor did not. This results suggest that codecoration of SnO_2 nanorods with Pd and ZnO improves the selectivity of the SnO_2 nanorod sensor as well as the sensitivity and sensing time.

4 Conclusions

The ZnO/Pd-codecorated SnO_2 nanorod sensor showed a stronger and faster response to NO_2 compared with ZnO or Pd-decorated SnO_2nanorod sensors.The former also showed higher selectivity than the latter. SEM images showed that Pd and ZnO did not contact each other in the ZnO/Pd-codecorated SnO_2nanorods. Therefore, a critical difference between the pristine and codecorated SnO_2 nanorod is the existence of Pd–SnO_2 and ZnO–SnO_2 interfaces in the latter. Two electronic sensing mechanisms resulting from the existence of these n–n junctions, i.e., modulation of the depletion layer width or conduction channel width at the heterojunction interface, and modulation of the interfacial potential barrier height, should be considered when explaining the enhanced sensing performance of the Pd and ZnO-codecorated SnO_2 nanorod sensor. On the other hand, the chemisorption and dissociation of NO_2 gas is enhanced on the Pd nanoparticle surface and NO_2 gas is spilt over the Pd nanoparticles due to the highly catalytic or conductive nature of Pd. In addition, localized surface plasmons form in the Pd nanoparticles at the surfaces of Pd-decorated SnO_2 nanorods. Electrons are transferred from the localized surface plasmons in the Pd nanoparticles to the conduction band of the SnO_2 nanorods. Consequently, the number of electrons attracted to the gas is increased by Pd decoration, leading to the enhanced electrical response of the nanorod sensor to the gas.

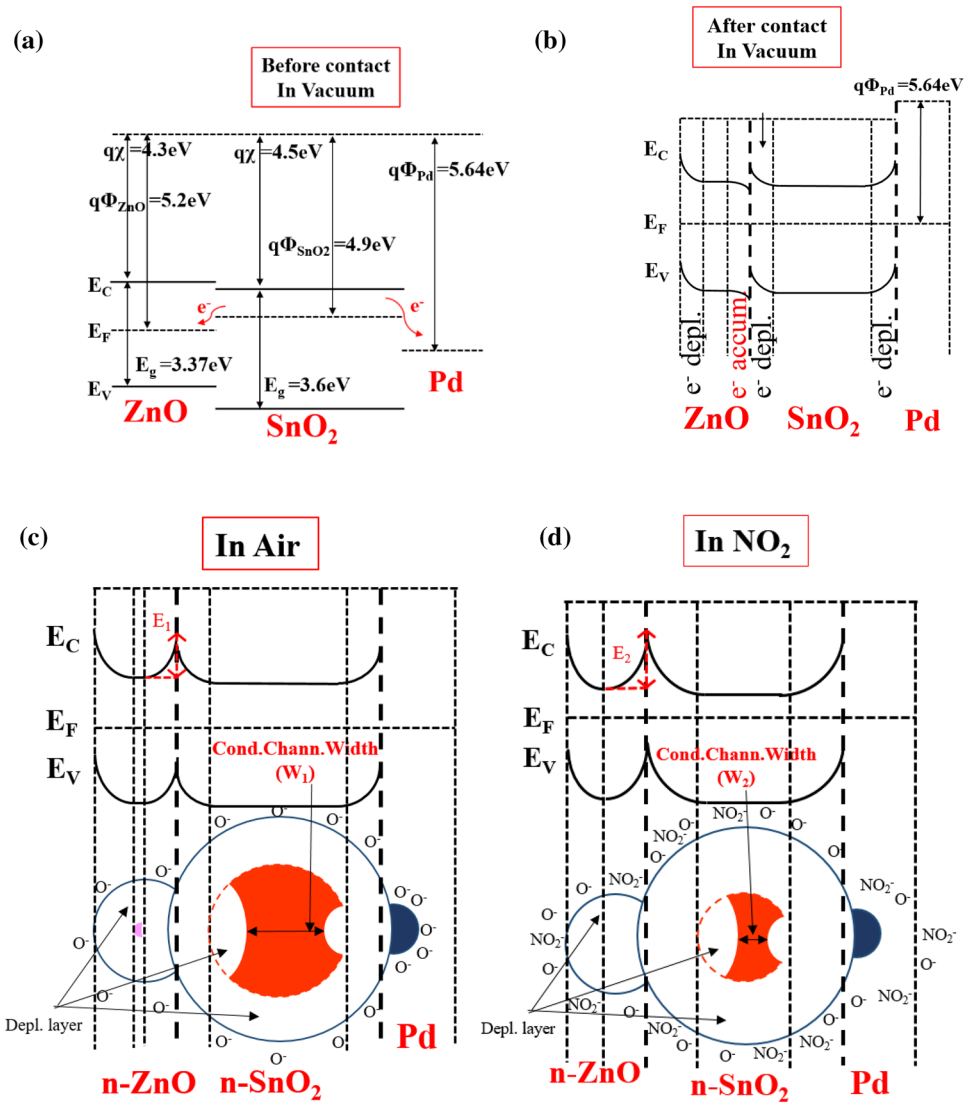

Fig. 7 Energy band diagrams of an SnO–ZnO couple: **a** before contact in vacuum, **b** after contact in vacuum, **c** after contact in air, an$_2$d **d** after contact in NO_2 at 300 °C

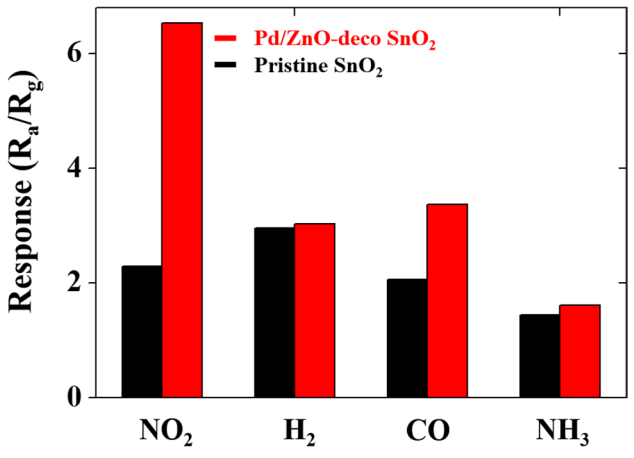

Fig. 8 Comparison of the responses of the pristine SnO_2 nanorods and Pd-decorated SnO_2 nanorods to various gases of 5 ppm including NO_2

Acknowledgements This study was supported by Basic Science Research Program through the National Research Foundation of Korea (NRF) funded by the Ministry of Education (nos. 2015R1D1A1A01057029 and 2010–0020163).

References

1. M. Penza, C. Martucci, G. Gassano, Sens. Actuators B **50**, 52–59 (1998)
2. K. Wetchakun, T. Samerjai, N. Tamaekong, C. Liewhiran, C. Siriwong, V. Kruefu, A. Wisitsorat, A. Tuantranont, S. Phanichphant, Sens. Actuators B **160**, 580–591 (2011)
3. N.D. Hoa, S.A. El-Safry, Chem. Eur. J. **17**, 12896–12901 (2011)
4. T.J. Hsueh, S.J. Chang, C.L. Hsu, Y.R. Lin, I.C. Chen, Appl. Phys. Lett. **91**, 053111–053111 (2007)
5. M.S. Wagh, G.H. Jain, D.R. Patil, S.A. Patil, L.A. Patil, Sens. Actuators B **115**, 128–133 (2006)
6. J. Wollenstein, J.A. Plaza, C. Cane, Y. Min, H. Bottner, H.L. Tuller, Sens. Actuators B **93**, 350–355 (2003)
7. S. Mridha, D. Basak, Semicond. Sci. Technol. **21**, 928–932 (2006)

8. Y. Sun, N.G. Ndifor-Angwafor, J.D. Riley, M.N.R. Ashfold, Chem. Phys. Lett. **431**, 352–357 (2006)
9. Y. Kolmakov, G. Zhang, M. Cheng, Moskovits, Adv. Mater. **15**, 997–1000 (2003)
10. Y. Liu, E. Koep, M. Liu, Chem. Mater. **17**, 3997–4000 (2005)
11. F. Chaabouni, M. Abaab, B. Rezig, Sens. Actuators B. **100**, 200–204 (2004)
12. Q. Wan, T. Wang, Chem. Commun. **1**, 3841–3843 (2005)
13. H. Kim, C. Jin, S. Park, S. Kim, C. Lee, Sens. Actuators B **161**, 594–599 (2012)
14. A. Kolmakov, D.O. Klenov, Y. Lilach, S. Stemmer, M. Moskovits, Nano Lett. **5**, 667–673 (2005)
15. T. Rakshit, S.P. Mondal, I. Manna, S.K. Ray, ACS Appl. Mater. Interfaces **4**, 6085–6095 (2012)
16. C.W. Na, H.-S. Woo, I.-D. Kim, J.-H. Lee, Chem. Commun. **47**, 5148–5150 (2011)
17. G.J. Sun, J.K. Lee, S.B. Choi, W.I. Lee, H.W. Kim, C. Lee, ACS Appl, Mater. Interfaces **9**, 9975–9981 (2017)
18. S. Park, S. An, Y. Mun, C. Lee, ACS Appl. Mater. Interfaces **5**, 4285–4292 (2013)
19. N. Singh, A. Ponzoni, R.K. Gupta, P.S. Lee, E. Comini, Sens. Actuators B **160**, 1346–1351 (2011)
20. S.-W. Choi, A. Katoch, J.-H. Kim, S.S. Kim, J. Mater. Chem. C. **3**, 1521–1527 (2015)
21. B.S. Min, Y.H. Park, C.S. Lee, J. Nanosci Nanotechnol. **14**, 8495–8501 (2014)
22. A. Srivastava, K. Jain, Mater. Chem. Phys. **105**, 385–390 (2007)
23. J.H. Kim, H.W. Kim, S.S. Kim, Sens. Actuators B **239**, 578–585 (2017)
24. M. Bonyani, J.K. Lee, G.J. Sun, S. Lee, S.T. Ko, C. Lee, Thin Solid Films **636**, 257–266 (2017)
25. K. Lee, W.S. Lee, S.K. Hyun, C. Lee, Phys. Status Solidi A **215**, 1700929 (2018)
26. S. Rudeerat, Bull. Mater. Sci. **38**, 1033–1038 (2015)
27. K. Nejati, Z. Rezvani, R. Pakizevand, Int. Nano Lett. **1**, 75–81 (2011)
28. S. Park, S. An, H. Ko, S. Lee, C. Lee, Sens. Actuators B **188**, 1270–1276 (2013)
29. N. Barsan, U. Weimar, J. Electroceram. **7**, 143–167 (2001)
30. T.V. Belysheva, L.P. Bogovtseva, E.A. Kazachkov, N.V. Serebryakova, J. Anal. Chem. **58**, 583–587 (2003)
31. R. Ferro, J.A. Rodriguez, P. Bertrand, Thin Solid Films **516**, 2225–2230 (2008)
32. N.H. Kim, H.W. Kim, C. Seoul, C. Lee, Mater. Sci. Eng. B **111**, 131–134 (2004)
33. M. Boudart, J. Mol. Catal. A: Chem. **138**, 319–321 (1999)
34. D.O. Kolmakov, Y. Klenov, S. Lilach, M. Stemmer, Moskovits, Nano Lett. **5**, 667–673 (2005)
35. A.J. Du, S.C. Smith, X.D. Yao, G.Q. Lu, J. Am. Chem. Soc. **129**, 10201–10204 (2007)
36. G. Jimenez-Cadena, J. Riu, F.X. Rius, Analyst **132**, 1083–1099 (2007)